Applied Catalysis B: Environmental 132–133 (2013) 54–61

Contents lists available at SciVerse ScienceDirect

Applied Catalysis B: Environmental

journal homepage: www.elsevier.com/locate/apcatb

Selective hydrogenation of CO_2 and CO to useful light olefins over octahedral molecular sieve manganese oxide supported iron catalysts

Boxun Hu[a], Samuel Frueh[b], Hector F. Garces[a], Lichun Zhang[a], Mark Aindow[a], Christopher Brooks[c], Eric Kreidler[c], Steven L. Suib[a,b,*]

[a] Institute of Material Science, University of Connecticut, Storrs, CT 06269, USA
[b] Department of Chemistry, University of Connecticut, Storrs, CT 06269, USA
[c] Honda Research Institute USA, Inc. 1381 Kinnear Road, Suite 116, Columbus, OH 43212, USA

ARTICLE INFO

Article history:
Received 22 May 2012
Received in revised form
11 September 2012
Accepted 2 November 2012
Available online 27 November 2012

Keywords:
Carbon dioxide utilization
DART
Olefin
Fischer-Tropsch
Manganese oxide

ABSTRACT

Porous cryptomelane-type octahedral molecular sieve manganese oxide (K-OMS-2) supported iron nanocatalysts have been developed for selective hydrogenation of CO_2 and CO to light olefins. Surface coated iron (SCI) catalysts and frame-work doped iron (FDI) catalysts have different interfaces. The synergistic interactions of nano-size iron carbides, potassium promoters, and manganese oxides vary in these two types of the Fischer-Tropsch (F-T) catalysts with respect to their catalytic activities and selectivity. For example, the SCI catalysts have high selectivity (>95%) to light olefins but low catalytic activity with a CO conversion of 45% and a CO_2 conversion of 32%. The FDI catalysts showed higher catalytic activities with a CO conversion of 87% and a CO_2 conversion of 45%. Direct analyses in real time-mass spectra and temperature programmed reduction-mass spectra have been used to correlate temperature effects. These component–structure–activity relationships provide insight for CO_2 utilization and F-T syntheses.

1. Introduction

Environmental concerns about the increase of CO_2 emissions have spurred the exploration of CO_2 utilization [1]. CO_2 conversion to useful compounds provides a viable solution for CO_2 utilization [2–4]. Light olefins (C_2–C_6) are in high demand in the polymer, pharmaceutical, and chemical industries. Ethylene and propene are largely produced by cracking of naphtha, ethane, and propane. Oligomerizations of methane, ethylene, and propene also provide synthesis methods for light olefin production [5,6]. Fischer-Tropsch (F-T) synthesis has provided a method for fuel production using syngas (CO/H_2) from coal, natural gas, and biomass [7,8]. This process has recently regained interest for selective production of value-added light olefins not only from CO but also from the greenhouse gas CO_2 [9–11]. Selective catalysts are the key for the F-T synthesis.

Both iron and cobalt catalysts are good commercial F-T catalysts. Iron catalysts are favored due to their higher selectivity to light olefins, lower cost, commercial availability, and tolerance to high temperatures and moisture environments [12]. Al_2O_3 and SiO_2 supported iron catalysts have been reported for light olefin production with a carbon selectivity of 53% (CO_2 excluded) at 613 K and 20 Mpa [9]. High reaction temperature leads to carbon deposition and the formation of excess CO_2 in CO hydrogenation. In the search for catalysts for olefin production, catalysts containing Fe–Mn–K have been favored since 1980s. Venter et al. reported amorphous carbon supported K–Fe–Mn carbonyl catalysts with a selectivity of 85–90 wt% to C_2–C_4 olefins [13]. But the catalytic activity is low with a CO conversion of 1.4%. Li et al. reported impregnated Fe–Mn–K catalyst on SiO_2 with a CO conversion of 51.9% and a selectivity of 36.7% to C_2–C_4 olefins [14]. Barrault and Renad found that MnO supported Fe catalysts have great production of C_2–C_4 olefins and methane inhibition at 573 K and 1 Mpa [15]. These studies suggest that the locations of Fe and Mn significantly affect the selectivity and activity of the catalysts.

To compare the distinct results of the two Fe–Mn–K interaction systems, the catalyst compositions and reaction conditions must be similar. We developed two new F-T catalysts: frame-work doped iron (FDI) catalysts and surface coated iron (SCI) catalysts, which have the similar compositions of Fe, Mn, and K, and they have been tested under the same F-T conditions. In this study, unique nanofiber supports ($KMn^{3+}Mn_7^{4+}O_{16}$) have been used for the F-T catalysts. They are composed of 2×2 edge-shared MnO_6^- octahedral chains, which are corner shared to form one-dimensional

* Corresponding author at: Department of Chemistry, University of Connecticut, Unit 3060, 55 North Eagleville Road, Storrs, CT 06269-3060, USA. Tel.: +1 860 486 2797; fax: +1 860 486 2981.
E-mail address: steven.suib@uconn.edu (S.L. Suib).

0926-3373/$ – see front matter © 2012 Elsevier B.V. All rights reserved.
http://dx.doi.org/10.1016/j.apcatb.2012.11.003

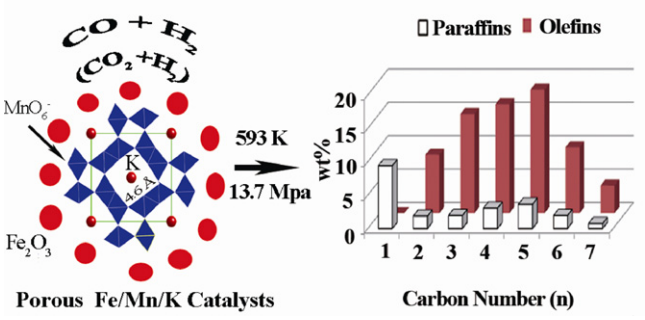

Fig. 1. Illustrations of K-OMS-2 supported iron catalysts and their high selectivity to olefins in F-T syntheses.

tunnels, and K^+ ions are located in the tunnels (Fig. 1) [16]. Iron catalysts are located in the catalyst framework (FDI) or on the surfaces of K-OMS-2 nanofibers (SCI). Each component contributes to the catalytic activity and selectivity to light olefins. Potassium and manganese components are promoters, which enhance catalyst activity and selectivity to light olefins [17–19]. K-OMS-2 is an excellent dehydrogenation catalyst for selective production of olefins [20]. K-OMS-2 supported iron catalysts showed very high activity and selectivity to light olefins in the F-T synthesis (Fig. 1). These new iron catalysts have not ever been reported in the F-T synthesis.

The structure–activity relationships of the new F-T catalysts have been investigated using transmission electron microscopy (TEM) and online gas chromatograph (GC). TEM images and GC results shows that the FDI catalysts have higher catalytic activity than the SCI catalysts due to highly dispersed Fe–MnO interfaces in the FDI catalysts. In addition, porous catalysts have a tendency for strong re-adsorption of light olefins. Direct analyses in real time-mass spectra (DART MS) have shown strong re-adsorption of light olefins on the post CO_2 hydrogenation catalysts. This olefin adsorption may change the carbon chain growth mechanisms, and combined with potassium and manganese promotion effects in the complex catalytic reactions, lead to carbon chain growth of these catalysts that shows deviated Anderson–Schulz–Flory (ASF) distributions. The selectivities to light olefins (C_3–C_6) increase. These structure–activity relationships affecting the catalytic selectivity and activity are discussed in this study.

2. Experimental

2.1. Catalysts preparation

The K-OMS-2 supports were prepared by a hydrothermal method which is described elsewhere [21]. A total of 64 mmol of $MnSO_4$, $K_2S_2O_8$, and K_2SO_4 in a molar ratio of 2:3:3 were mixed with deionized (DI) H_2O (70 mL) in a 125 mL autoclave; then the autoclave was sealed in an acid digestion bomb and placed in an oven (453 K) for 12 h. As-synthesized K-OMS-2 was used for the preparation of the SCI catalysts using an incipient wetness impregnation method [22]. K-OMS-2 (3.05 g), $Fe(NO_3)_2{\cdot}H_2O$ (2.91 g), and DI water (150 mL) were stirred in a 400 mL beaker at 348 K until water was evaporated. After being dried overnight in a 393 K oven, the SCI catalysts (noted as CAT A) with a Fe/Mn weight ratio of 1/5 were used in the F-T synthesis.

The FDI catalysts with the same Fe/Mn (1/5) ratio were synthesized using a modified method [23]. $MnCl_2{\cdot}4H_2O$ (5.63 g) and $FeCl_3{\cdot}6H_2O$ (7.68 g) were dissolved in 150 mL of DI water. Oxygen (0.5 L/min) was bubbled into the solution with stirring. A solution containing of 15 g of NaOH in 60 mL of DI water was then added dropwise to the solution. The products were filtered and washed using 1 L DI water. Then the products were ion-exchanged with 150 mL KCl (9.31 g) solutions, and then the products were filtered and washed with 1 L DI water again. Fe–K–birnessite was formed. And then, Fe–K–birnessite (6.25 g), K_2SO_4 (5.85 g), and DI water (70 mL) reacted at 453 K for 24 h in an acid digestion bomb, the products were filtered, washed, and dried for the F-T synthesis. This sample was noted as CAT B.

2.2. Catalyst characterization

Powder XRD experiments were performed with a Scintag XDS 2000 X-ray diffractometer equipped with a Cu Kα X-ray source. Field emission scanning electron microscopy (FESEM) was performed using a Zeiss DSM 982 Gemini FESEM instrument with a Schottky emitter. TEM images were obtained using a JEOL 2010 FasTEM at accelerating voltages of 200 kV. A Micromeritics ASAP 2010 instrument was used to measure BET surface area using nitrogen adsorption at 77 K. Temperature programmed reduction mass spectrometry (TPR-MS) analysis was performed with a home-made setup and an MKS-UT1 PPT quadrupole mass spectrometer. A Perkin Elmer 3110 AA spectrometer was used for atomic absorption (AA) analysis of the catalyst compositions [24]. The sulfur contents of catalyst surfaces were analyzed with X-ray photoelectron spectroscopy (XPS) analysis performed on a PHI 595 multiprobe system.

In situ DART MS have been used for the characterization of the adsorbed species on post-reaction catalysts. DART MS experiments have been performed in a nitrogen environment using an AccuTOF instrument using a home-made glove box. This fast and non-destructive analysis method is described elsewhere [25]. The DART ion source was coupled to an AccuTOF orthogonal time-of-flight (TOF) mass spectrometer. The orifice of an atmospheric pressure interface was set to 30 eV. The exit electrode was held at 300 V, and the corona discharge voltage was 3000 V. Helium (2.8 L/min) was used as the corona discharge gas and was heated at 623 K. The post-reaction catalysts was attached to a wet glass rod and loaded into the gap (~1 cm) of the ion source and the TOF inlet.

2.3. Hydrogenation of CO_2 and CO

Catalysts (0.75 g) were loaded into a packed stainless steel tube reactor (ID 0.9 cm). The catalysts were heated in 10% CO/He (balance) to 723 K (unless noted) in a tube furnace at a ramp rate of 5 K/min. The catalysts were reduced for 6 h. For comparison, some CO_2 hydrogenation catalysts were also reduced in 10% H_2/He following the same procedures. Hydrogenations of CO_2 or CO were performed in a packed bed reactor [26] at temperatures of 393–593 K and a pressure of 13.7 Mpa. Pre-mixed high pressure $CO_2/H_2/Ar$ (Gas 1, ratio 3:6:1) and $CO/H_2/Ar$ (Gas 2, 3:6:1) gas mixtures (Airgas) were used for FT syntheses. Argon was an internal standard for GC analysis. After each F-T test, the reactor and tubes were washed using ethanol and water to avoid cross-contamination, and dried at 120 °C for 12 h. Then, the purging gas (N_2) from the reaction system was analyzed with a GC to make sure that no residues were present.

Gaseous products were analyzed using an online GC (SRI 8610C) equipped with a flame ionization detector and a thermal conductivity detector in series. The detection limit of the GC is about 200 ppm. Condensed liquid products were analyzed by a modified GC–MS method [24].

3. Results

3.1. Catalyst structure, compositions, and morphologies

The structure and phase purity of these catalysts have been identified from their XRD patterns (Fig. 2). K-OMS-2 supports are pure

Table 1
The compositions and BET data of the K-OMS-2 supported iron catalysts and Co/Mn_2O_3 reference catalysts.

Samples	BET SA (m^2/g)	Pore volume (cm^3/g)	AA analysis results (atomic %)			
			Mn	K	Fe	O
K-OMS-2	70.5	0.23	32.1	4.0	0	63.9
CAT A	65.6	0.19	29.1	3.9	5.8	61.4
CAT B	70.3	0.25	28.3	4.3	5.7	61.7
Co/Mn_2O_3	9.0	0.05	32.8	0	(Co: 8.8)	58.4

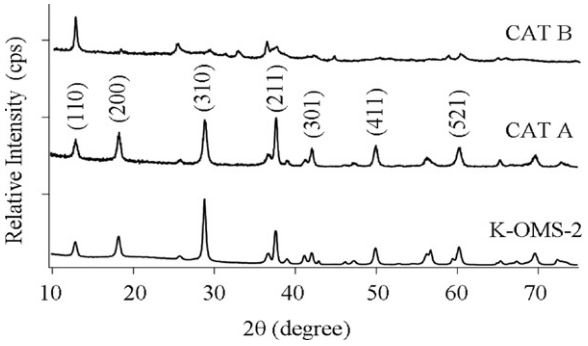

Fig. 2. The XRD patterns of CAT A, CAT B, and the K-OMS-2 supports.

tetragonal phase (JCPDS No. 29–1020) with the cryptomelane-type structure. Both SCI and FDI catalysts show an identical structure to that of K-OMS-2. The XRD pattern of FDI catalysts shows peak broadening. The crystallite size of catalysts along the [2 0 0] direction was calculated from the Scherrer Equation. The crystallite size of the CAT B (5.2 nm) is smaller than that of CAT A (17.7 nm) and K-OMS-2 (15.5 nm). The crystallite sizes of these catalysts were increased 2–3 times after reaction due to sintering. A strong (1 1 0) peak of the CAT B catalysts and the existence of 4.3% K^+ in the CAT B catalysts (Table 1) indicate an impurity phase of Fe–K–birnessite.

The K-OMS-2 supports are porous one-dimension nanofibers with a diameter of 20–50 nm (Fig. 3) and a length of more than 0.5 μm. The pore volumes of tunnel-structured K-OMS-2 are 0.19–0.23 cm^3/g (Table 1). K-OMS-2 supports and their supported catalysts have high BET surface areas (SA) of 65.6–70.5 m^2/g. These K-OMS-2 supports contains 4 atomic% of K^+ ions in the tunnel structure. Atomic absorption analyses show that Fe and Mn concentrations in the catalysts were very close due to careful control of the Fe/Mn/K ratios in the reactants. Reported porous microsize Mn_2O_3 supported Co catalysts (Table 1) are used as reference catalysts [27]. These potassium-free catalysts were compared with more porous K-OMS-2 supported catalysts.

The surface sulfur contents on K-OMS-2 supports (pre-test and post-test) catalysts have been examined by XPS because the sulfate salts were used in catalyst preparation. The sulfur contents on these K-OMS-2 and catalysts were under the detection limit of XPS (~500 ppm). The sulfur contents of these catalysts were under the detection limit of DART TOF MS (~10 ppm).

The high resolution TEM images of Fig. 3 show the nanostructure of CAT A and CAT B catalysts. The differences between CAT A and CAT B catalysts are clearly shown in the TEM images. For the CAT A catalysts, nanofilms of Fe_2O_3 nanoparticles were coated along the K-OMS-2 nanofibers after the IWI process. The coated Fe_2O_3 nanoparticles are in the size range of 5–25 nm. The *d*-spacing of 1.09 nm is assigned to the (6 4 2) planes of Fe_2O_3. This is consistent to the report that the main phase of the catalyst prepared from ferric nitrate is Fe_2O_3 [28]. The *d*-spacing of 0.69 nm is assigned to the (1 1 0) planes of K-OMS-2. For the CAT B catalysts reduced in H_2, Iron comes from framework-doped Fe-K-OMS-2. The Fe ions near the surface of Fe-K-OMS-2 was first reduced and diffused on the surface. The *d*-spacing (2.0 Å) of the (1 1 0) planes of α-Fe in the TEM image shows the existence of Fe. Iron is then converted to iron carbide-an active phase in the F-T synthesis [7,29]. These well dispersed iron catalysts formed many FeC_x–MnO catalytic interfaces (Fig. 3D). These catalytic interfaces play important roles in the formation of light olefins [30].

3.2. Catalytic activity and selectivity in CO_2 and CO hydrogenation

3.2.1. CO hydrogenation

The CAT A and CAT B catalysts show very different results in CO hydrogenation. The comparisons of CAT A, CAT B, and similar existing catalysts are listed in Table 2. The CAT B catalysts show much higher catalytic activity than the CAT A catalysts. But the CAT A catalysts show much higher selectivity to olefins than the CAT B catalysts. Compared to the previously reported $Mn_{0.24}FeK_{0.08}$ (Li et al. [14]) and $Fe_{30}K_2Cu_{3.75}$ catalysts (Pirola et al. [31]), both CAT A and CAT B catalysts show higher selectivities to olefins, and CAT B catalysts show the highest activity.

The chain growth and product distributions were evaluated with an ASF kinetic model: [32]

$$W_n/n = (1-\alpha)^2\alpha_n{}^{-1} \quad (1)$$

where W_n is the weight fraction of hydrocarbon molecules containing *n* carbon atoms, α is the chain growth probability, and the values of α were calculated from the slope of a plot of logarithm of W_n/n versus *n*. Compared to microsize Mn_2O_3 supported Co catalysts [27], the carbon chain growth on both CAT A and CAT B catalysts showed non-ASF distributions in CO hydrogenation (Fig. 4). The CAT B catalysts showed a more deviated ASF distribution than the CAT A catalysts. More C_3–C_6 olefins were produced than that expected from the ASF distribution (Fig. 5).

Table 2
Comparisons of OMS-2 supported Fe catalysts with existing catalysts for CO hydrogenation.

Catalysts	GHSV (h^{-1})	CO conv. (%)	Selectivity (%)				Data sources
			CO_2	CH_4	C_{2+}	C=/C—	
CAT A	3360	25.6	28.2	13.6	58.2	13.4	This study
CAT B	3360	87.2	19.3	7.6	73.1	3.8	This study
$Mn_{0.24}FeK_{0.08}$	2000	51.9	NA	9.5	90.5	2.7	Ref. [14]
$Fe_{30}K_2Cu_{3.75}$	1965	38.1	32	6	62	NA	Ref. [31]

Note: GHSV: gas hourly space velocity. NA indicates that the reference did not provide the data. The reaction temperatures (same unless noted) were 593 K for CAT A/B, 523 K for Ref. [14], and 603 K for Ref. [31] respectively. The olefin/paraffin (C=/C—) ratio was calculated from C_2–C_6. The selectivity is based on carbon (C%).

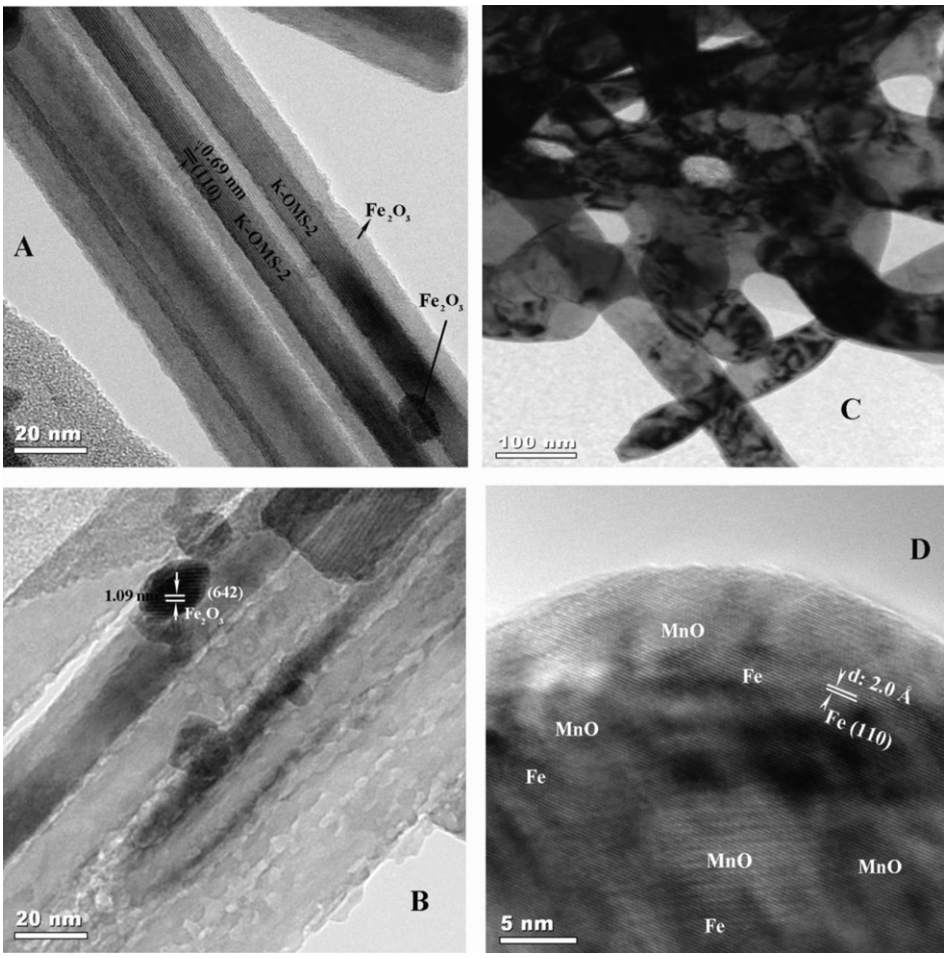

Fig. 3. The TEM images of the CAT A (A and B) and CAT B (C and D) catalysts (reduced by H_2).

3.2.2. CO_2 hydrogenation

CO_2 hydrogenation produces mostly methane. The production of higher hydrocarbon products from CO_2 hydrogenation is more difficult than from CO hydrogenation. The reverse water–gas shift reaction (RWGS, Eq. (1a)) is the first step for CO_2 hydrogenation.

$$CO_2(g) + H_2(g) \rightarrow CO(g) + H_2O(g) \quad (1a)$$

Table 3 shows that larger amounts of CO and CH_4 have formed on the H_2 reduced CAT B catalysts than the CO reduced CAT B catalysts, and while more light olefins have formed on the CO reduced CAT B catalysts than the H_2 reduced CAT B catalysts. The CO reduced CAT B catalysts have higher catalytic activity than the H_2 reduced CAT B catalysts. A high olefin/paraffin ratio is shown in the CO_2 hydrogenation products of CAT A like the CO hydrogenation products of CAT A. CO_2 hydrogenation products of these CAT A and CAT B catalysts do not follow an ASF distribution as that CO hydrogenation products, but the deviation of ASF distribution shown in Fig. 4B is not as large as that in Fig. 4A.

3.3. DART-MS and TPR-MS spectra

The adsorbed chemical species on the post-reaction iron catalysts provide information for the study of the catalytic selectivity and the chain growth in the F-T synthesis. The DART mass spectra of Fig. 6 show that each group of peaks shows a mass increment of 14, indicating the addition of a CH_2 group to these growing compounds. For the iron catalysts reduced at 723 K (HT), light olefins (C_3^{2-}–C_6^{2-}) are the dominated species on the HT reduced catalysts.

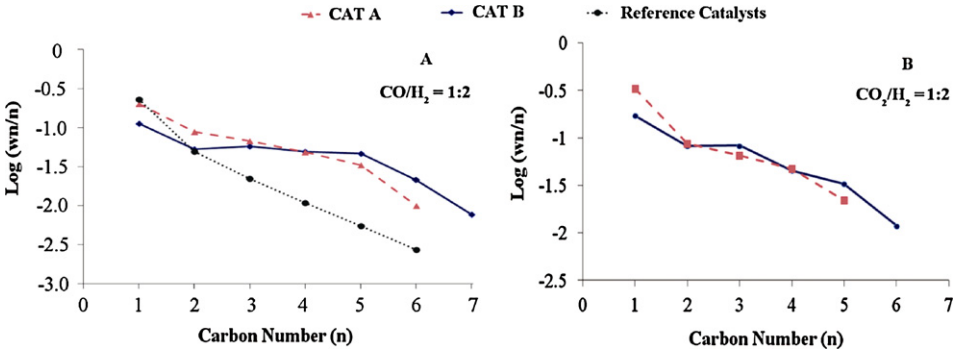

Fig. 4. The non-ASF plots of CAT A and CAT B in CO hydrogenation (A) and CO_2 hydrogenation (B).

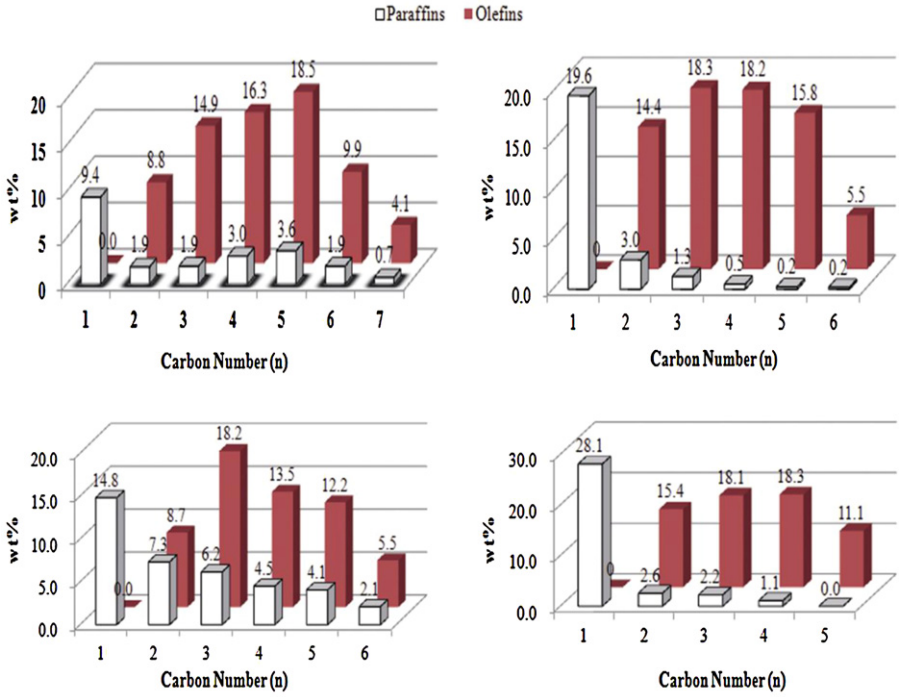

Fig. 5. The high selectivity of the K-OMS-2 supported catalysts to light olefins. (A) CAT B in CO hydrogenation, (B) CAT A in CO hydrogenation, (C) CAT B in CO_2 hydrogenation, (D) CAT A in CO_2 hydrogenation.

Table 3
Comparisons of OMS-2 supported Fe catalysts with existing catalysts for CO_2 hydrogenation.

Catalysts	GHSV (h^{-1})	CO_2 conv. (%)	Selectivity (%)				Data sources
			CO	CH_4	C_2–C_6	C=/C—	
CAT A[a]	3360	12.2	42.4	34.4	23.2	4.6	This study
CAT A[b]	3360	27.2	21.5	22.1	56.4	11.2	This study
CAT B[a]	3360	18.3	41.1	33.8	25.1	1.8	This study
CAT B[b]	3360	45.0	19.2	12.1	68.7	2.9	This study
CoFe	3000	28.4	5.2	34.5	60.3	1.2	Ref. [11]

The reaction temperature is 533 K for Ref. [11].
[a] Reduced with H_2/He.
[b] Reduced with CO/He.

Compared to the iron catalysts reduced at 623 K (LT), C_2–C_4 carboxylic acids are the dominant species on the LT reduced catalysts. The adsorbed species are consistent with the analyzed gas products by GC and the liquid products by GC–MS.

TPR-MS spectra of the K-OMS-2 support (Fig. 6C) show the selective production of carboxylic acids and olefins at LT and HT, respectively. This is because reduced K-OMS-2 supports at different temperatures show different abilities to supply oxygen [33]. The relative ease with which oxygen species can be released from K-OMS-2 implies higher oxidation activity. The LT reduced catalysts can release oxygen species to oxidize intermediate F-T products and form carboxylic acids. The HT reduced K-OMS-2 supports do not further lose lattice oxygen and the formed light olefins are less likely to be oxidized by the supports.

4. Discussion

Light olefin production, such as ethylene production, is often used as an index for the evaluation of the development of the petrochemical industry. Traditional light olefin production based on the oil industry has been challenged by depleting oil resources and increasing oil prices. Coal gases, shale gases, biomass, and even CO_2 could be substituted resources for olefin production. The F-T synthesis provides a process for olefin production using these alternate and abundant resources. Selective, efficient, and low cost catalysts are the key for practical production. The interfaces of the Fe–Mn–K catalysts are interesting for studying the F-T synthesis because they are the catalytic sites. In this study, doped iron catalysts and supported iron catalysts have been compared as two typical catalyst structures, which represent two distinct catalytic interfaces. The component–structure–activity relationships, size effects, and mechanisms are discussed in the following sections.

4.1. Component–structure–activity relationships

K-OMS-2 ($KMn^{3+}Mn_7{}^{4+}O_{16}$) is a unique support, which is porous and mixed-valent nanofibers with high surface areas. K-OMS-2 plays multiple functions in F-T syntheses. Firstly, high surface area K-OMS-2 supports disperse the catalytic sites and remove heat from reaction sites to alleviate the aggregation of nanocatalysts to keep the catalyst active. CO hydrogenation is a highly exothermic reaction. K-OMS-2 performs as traditional inert supports (Al_2O_3 and SiO_2) for dispersing catalysts and removing reaction heat. Secondly, K-OMS-2 provides manganese promoters, which are excellent promoters for light olefin production [34]. Different from existing co-precipitated Mn–Fe–K catalysts, the interfaces of these

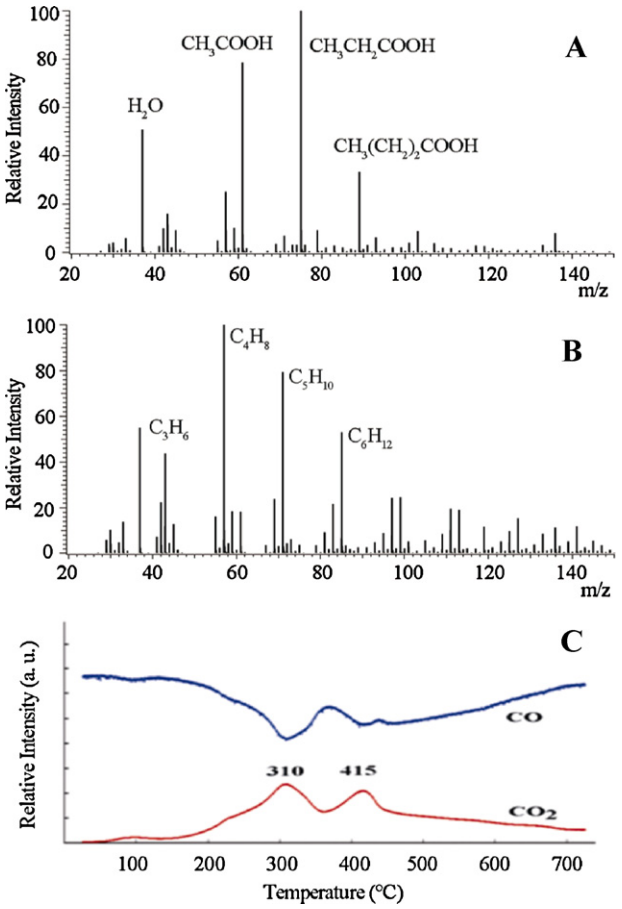

Fig. 6. DART TOF mass spectra (A and B) of adsorbed chemical species on post-reaction catalysts and TPR-MS spectra of the K-OMS-2 support using 5% CO/H_e (balance). (A) CAT A reduced at 623 K, (B) CAT A reduced at 723 K. The H_2O peak is due to wet glass rods.

K-OMS-2 supported Fe catalysts make Fe catalytic sites that are exposed to CO, CO_2, and H_2. Mn/K promoters are mostly located in internal sites of catalyst supports. This new design of catalytic interfaces improves the catalytic activity by alleviating the coverage of Fe catalytic sites by excess Mn and K, which hinder the adsorption of H_2 [14]. Thirdly, K^+ ions in K-OMS-2 act as promoters for chain growth and also improve the catalytic activity [18,35].

The SCI (CAT A) and FDI (CAT B) catalysts have different catalytic interfaces (Fig. 3) formed by IWI methods and hydrothermal methods, respectively. Most Fe catalysts in CAT A catalysts are located at the surface of K-OMS-2 nanofibers and are not incorporated into manganese oxide like the CAT B catalysts and other existing $Mn_{0.24}FeK_{0.08}$ catalysts prepared by co-precipitation and impregnation methods (Li et al. [14]). For the two different interfaces, the CAT A catalysts show higher selectivity to light olefins, indicating the strong interactions of Mn–Fe interfaces. But the catalytic activity of CAT A is much lower than that of CAT B. Several affecting factors, such as catalytic interfaces, iron carbide phases, particle sizes, adsorbed sulfate, and chloride ions change the catalytic activity and selectivity.

The Fe–MnO_x catalysts are very active in RWGS reaction (Eq. (1)) at about 573 K [36]. The Fe doped CAT B catalysts have more interactive interfaces of Fe–MnO_x than the Fe coated CAT A catalysts. The CAT B catalysts significantly reduce the CO_2 contents (19.3%) in the products than that (28.2%) of the CAT A catalysts. Metallic iron exists at the (H_2) reduced catalyst surfaces. More importantly, metallic iron converts to more active iron carbides when activated with CO/He. F-T reaction proceeds at imperfections on the surfaces of iron carbide and at interfaces with "islands" of Lewis acidic MnO_x promoters [30]. The K-OMS-2 reduction at different temperatures changes the Lewis acidity of MnO_x, resulting in the catalytic selectivity change from carboxylic acids (623 K) to light olefins (723 K) (Fig. 6). The CAT B catalysts are highly active in both CO and CO_2 hydrogenation with a CO conversion of 87% and a CO_2 conversion of 45%. These conversions are significantly higher than similar $Mn_{0.24}FeK_{0.08}$ and $FeK_2Cu_{3.75}$ catalysts in terms of CO conversion (51.9%). More importantly, these new catalysts have a higher selectivity (C^{2-}/C^-: 13.4 vs. 2.7) to valuable light olefins. Such FDC catalysts have exhibited good stability (about 10% of activity loss) in 144 h continuous tests.

The effects of sulfate (SO_4^{2-}) and chloride (Cl^-) ions on catalytic activity are largely dependent on their concentrations. There is no consensus on these anion effects. Addition of SO_4^{2-} to the catalyst improved the FTS activity at a sulfur loading of 0.05–0.80 g per 100 g Fe [37]. But other researchers report that a 500 ppm level of SO_4^{2-} or Cl^- resulted in the reduction of catalytic activity due to a decrease of the contents of α-Fe and Fe_3C; and the influence of SO_4^{2-} or Cl^- could be ignored if their concentration is lower than 50 ppm [38]. Our catalysts were carefully washed by DI water. The adsorbed SO_4^{2-} or Cl^- anions are below 50 ppm as shown in DART TOF MS and XPS analyses.

The particle sizes of nanocatalysts and supports affect hydrocarbon chain growth. Jong and Holmen found that the surface coverages of the CH_x, OH_x and CO intermediates decreased for small Co particles (<6 nm) and appeared to be constant for large particles, and while hydrogen coverage on small Co particles increased [39]. Therefore, smaller catalysts (<6 nm) have low activity and form higher CH_4 content. In Tables 1 and 2, CAT A (~2–7 nm Fe_2O_3) produced much more CH_4 (22.1%) in CO_2 hydrogenation than that (12.1%) of CAT B (~100 nm). The same trend occurs for CO hydrogenation (13.6% CH_4 for CAT A and 9.5% CH_4 for CAT B). The activity of CAT B is 2.4 times higher than that of CAT A in CO hydrogenation. The effect of sulfur and chloride was excluded above. These suggest that highly active F-T catalysts require optimal sizes. Reaction kinetics also affects the CH_4 content. In multiple-step reactions, if the reverse water–gas shift reaction is the rate determining step (slow), CO will convert to CH_4, a low CO and high CH_4 concentrations are presented. When the reaction temperature is high, CO hydrogenation is the rate determining step, a high CO and low CH_4 concentrations are found in Table 3.

The Mn and K promoters in K-OMS-2 cause secondary reactions in the F-T syntheses. Deviated ASF distributions are shown in Fig. 4 using CAT A and CAT B catalysts. Secondary reactions account for the non-ASF distributions. Several kinds of secondary reactions, including hydrocracking, isomerization [40], and chain initiation, have been described by Pechler et al. [41]. Specifically, potassium promotion reactions [18] (Eq. (2)), primary α-olefin reinsertion, and β-dehydrogenation (Eq. (3)) [42] are main secondary reactions using Mn and K promoted porous catalysts. In these experiments, β-dehydrogenation proceeds due to the dehydrogenation of manganese oxides. A cutoff of C_6 was observed using the CAT A catalysts. Compared with Mn_2O_3 supported catalysts (no potassium), addition of potassium promoters in CAT A and CAT B catalysts with more porous structures, and higher surface areas lead to non-ASF distributions (Table 1 and Fig. 4).

$$K_2CO_3(s) + CO(g) + H_2(g) \rightarrow 2HCOOK(l) \quad (2)$$

$$L_nM\text{-}H + CH_2{=}CH_2 \underset{\beta\text{-H elimination}}{\overset{\text{Olefin insertion}}{\rightleftharpoons}} L_nM\text{-}CH_2\text{-}CH_3 \xrightarrow{CH_2=CH_2} L_nM\text{-}CH_2CH_2CH_2CH_3 \quad (3)$$

(M: Fe, L: CO)

The porous structures of these catalysts could accelerate secondary reactions by the adsorption of more light olefins. Emmett and Iglesia have confirmed that primary α-olefins can be reinserted into the chain growth process by co-feeding studies [42,43]. These

porous supports increase the readsorption of olefins as shown in Fig. 6B. α-olefin reinsertion is observed in the CAT B catalysts, and high selectivities to C_3–C_5 olefins are shown in Fig. 5. These C_3–C_5 distributions are similar to that of mesoporous CoSi1 and CoSi7 catalysts [44]. Fewer long chain hydrocarbons (>C_{6+}) were produced here. The pore volumes (0.25 cm^3/g) and surface areas (70 m^2/g)) of these catalysts are much higher than that of the Mn_2O_3 supported catalysts (0.05 cm^3/g and 9.0 m^2/g, respectively). Higher pore volumes and surface areas may increase olefin readsorption and also secondary reactions. Kinetic models of FTS selectivity have been reported to explain these non-ASF product distributions (Fig. 4), and simulation results show fair agreement with experimental data [45,46].

4.2. Plausible mechanisms

The experiments of CO and CO_2 hydrogenation here have shown that iron carbide is the more active form of the iron catalyst than metallic iron as earlier reported results [47,48]. The Fe catalyst reduced in hydrogen without carbonization produced mainly CH_4 and C_2H_6 with a low CO_2 conversion of 18%. Similarly, Visconti et al. reported that Co/Al_2O_3 catalysts reduced in H_2/He produced 90% CH_4 at 493 K, and more CO (79%) was produced at 593 K [49]. In comparison to the CAT B catalysts after carbonization, CO_2 conversion increased to 45%. The CH_4 selectivity significantly decreased from 33.8% to 12.1% and C_{2+} hydrocarbon selectivity greatly increased from 25.1% to 68.7%.

Original carbide mechanisms propose the formation of the metal carbide followed by hydrogenation of the metal carbide to produce the products [7]. Density functional theory (DFT) calculations show that H_2 can easily cleave into adsorbed H and CH species on the Fe_3C (0 0 1) sites [50], and then they form CH_2, which is monomers for forming light olefins. The oxygenate mechanisms involving adsorption of CO and then hydrogenation have received more support since 1950. Emmett, Davis, and their coworker's experimental results have provided strong support for these mechanisms using C-tracer studies [51] and ethanol incorporation [52]. However, Emmett did not exclude metal carbides acting as intermediates.

The DART MS spectra of the adsorbed species on LT reduced iron catalysts are consistent with the adsorption model proposed by Kolbel and Tillmetz [53]. Porous manganese oxides also promote CO_2 adsorption. The chain initiation starts with CO_2 adsorbed on Fe–H to form adsorbed carboxylic acids (Eq. (4)). Oxygenates are protonated by DART ion sources to form C_2–C_4 carboxylic acids (Eq. (5)). This is clearly evidence for the participation of an oxygenate mechanism. These intermediates are similar to the key intermediates ($HCOO^-$, CO_3^{2-}, and $HOCO^-$) on Au (1 1 1) in the water–gas shift (WGS) reaction [54]. The reduced Fe–Mn–K catalysts are very active for reverse WGS reactions at 573 K [34,36]. The reverse WGS reaction (CO_2 hydrogenation) produces large amounts of CO (19.2–41.1%) and a high water concentration (1.23%) in CO_2 hydrogenation. For the LT reduced iron catalysts, the carburization process is incomplete compared to the HT reduced catalysts. Less Fe=CH_2 species form via carbide mechanisms, and this limits the carbon chain growth. Their catalytic activities are also low.

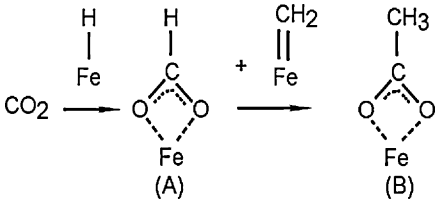

(4)

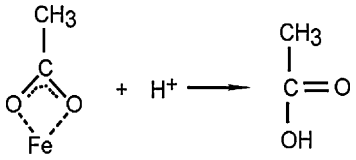

(5)

From the above hypothesis, the ratio of Fe_3O_4/Fe_3C (or other carbides) in the Fe–Mn–K catalysts may determine which mechanisms, carbide mechanisms or oxygenate mechanisms, dominate in these F-T syntheses. The quantitative characterization of Fe_3O_4/iron carbides has been recently reported by de Smit et al. [47] Mn and K allow an increase in the temperatures of reduction and carburization as compared to pure Fe_3O_4 without Mn and K promoters. In these Fe–Mn–K catalysts, few oxygenates exist even in HT reduced catalysts as shown in Fig. 6B.

5. Conclusions

In this study, new K-OMS-2 nanofiber supported Fe catalysts have been developed for light olefin production in both CO and CO_2 hydrogenation. The product distributions over the K-OMS-2 supported iron catalysts are similar in both CO_2 and CO hydrogenation. New K-OMS-2 supported iron catalysts have shown high selectivity to light olefins at a temperature of 593 K. Low temperature reduced catalysts led to C_2–C_6 carboxylic acids, and high temperature reduced catalysts increased the activity and selectivity to light olefins. The synergistic effect of iron carbides, potassium promoters, and manganese oxide supports contribute to high selectivities (C^{2-}/C^-: 1.8–13.4) and catalytic activities (87.2% CO conversion and 45% CO_2 conversion) in both CO hydrogenation and CO_2 hydrogenation.

The different catalytic interfaces of frame-work doped iron catalysts and surface coated iron catalysts show different results. The DART TOF MS data have shown strong adsorption of light olefin and carboxylic acids on the post-reaction iron catalysts for the catalysts reduced at HT and LT, respectively. These data suggested the existence of different reaction mechanisms. Non-ASF product distributions have been observed for these K-OMS-2 supported iron catalysts. The study of structure–composition–activity relationships provides new insight for the production of light olefins in CO_2 and CO hydrogenation.

Acknowledgments

This project was funded by the Chemical Sciences, Geosciences, and Biosciences Division of the Office of Basic Energy Sciences, and Office of Science, U.S. Department of Energy (under project DE-FGO2-86ER13622.A000) and Honda Research Institute, USA. Inc. We thank Dr. Heng Zhang for the XPS work, Dr. You-Jun Fu, Dr. Frank Galasso, and Dr. Raymond Joesten for helpful discussions.

References

[1] C. Song, Catalysis Today 115 (2006) 2–32.
[2] Y. Li, W.N. Wang, Z.L. Zhan, M.H. Woo, C.Y. Wu, P. Biswas, Applied Catalysis B 100 (2010) 386–392.
[3] J. Toyir, P.R. de la Piscina, J.L.G. Fierro, N. Homs, Applied Catalysis B 29 (2001) 207–215.
[4] B. Hu, V. Stancovski, M. Morton, S.L. Suib, Applied Catalysis A 382 (2010) 277–283.
[5] L.D. Conde, S.L. Suib, Journal of Physical Chemistry B 107 (2003) 3663–3670.
[6] F. Speiser, P. Braunstein, W. Saussine, Accounts of Chemical Research 38 (2005) 784–793.
[7] F. Fischer, H. Tropsch, Brennstoff-Chemie 7 (1926) 97–116.
[8] Q.H. Zhang, J.C. Kang, Y. Wang, Chemcatchem 2 (2010) 1030–1058.
[9] H.M.T. Galvis, J.H. Bitter, C.B. Khare, M. Ruitenbeek, A.I. Dugulan, K.P. de Jong, Science 335 (2012) 835–838.
[10] S.H. Kang, J.W. Bae, P.S. Prasad, S.J. Park, K.J. Woo, K.W. Jun, Catalysis Letters 130 (2009) 630–636.

[11] F. Tihay, A.C. Roger, G. Pourroy, A. Kiennemann, Energy and Fuels 16 (2002) 1271–1276.
[12] B.H. Davis, Industrial and Engineering Chemistry Research 46 (2007) 8938–8945.
[13] J. Venter, M. Kaminsky, G.L. Geoffroy, M.A. Vannice, Journal of Catalysis 105 (1987) 155–162.
[14] T. Li, Y. Yang, C. Zhang, Z. Tao, H. Wan, X. An, H. Xiang, Y. Li, Journal of Natural Gas Chemistry 16 (2007) 244–251.
[15] J. Barrault, C. Renad, Nouveau Journal de Chimie 7 (1983) 149–150.
[16] S.L. Suib, Accounts of Chemical Research 41 (2008) 479–487.
[17] Z.C. Tao, Y. Yang, C.H. Zhang, T.Z. Li, M.Y. Ding, H.W. Xiang, Y.W. Li, Journal of Natural Gas Chemistry 16 (2007) 278–285.
[18] M.D. Weisel, J.L. Robbins, F.M. Hoffmann, Journal of Physical Chemistry 97 (1993) 9441–9450.
[19] L.Y. Xu, Q.X. Wang, Y.D. Xu, J.S. Huang, Catalysis Letters 31 (1995) 253–266.
[20] L. Jin, J. Reutenauer, N. Opembe, M. Lai, D.J. Martenak, S. Han, S.L. Suib, Chemcatchem 1 (2009) 441–444.
[21] J. Yuan, K. Laubernds, J.C. Villegas, S. Gomez, S.L. Suib, Advanced Materials 16 (2004) 1729–1732.
[22] S. Sun, K. Fujimoto, Y. Zhang, N. Tsubaki, Catalysis Communications 4 (2003) 361–364.
[23] J. Cai, J. Liu, W.S. Willis, S.L. Suib, Chemistry of Materials 13 (2001) 2413–2422.
[24] B. Hu, C. Chen, S.J. Frueh, L. Jin, R. Joesten, S.L. Suib, Journal of Physical Chemistry C 114 (2010) 9835–9844.
[25] R.B. Cody, Analytical Chemistry 81 (2009) 1101–1107.
[26] M. Ojeda, R. Nabar, A.U. Nilekar, A. Ishikawa, M. Mavrikakis, E. Iglesia, Journal of Catalysis 272 (2010) 287–297.
[27] B. Hu, C. Brooks, E. Kreidler, S.L. Suib, Porous Metal Oxides as Catalysts, MRS Proceedings Spring, 2012, MRS, http://dx.doi.org/10.1557/opl.2012.956, in press.
[28] H. Hayakawa, H. Tanaka, K. Fujimoto, Catalysis Communications 8 (2007) 1820–1824.
[29] P. Biloen, W.M.H. Sachtler, Advances in Catalysis 30 (1981) 165–216.
[30] P.M. Maitlis, V. Zanotti, Chemical Communications 13 (2009) 1619–1634.
[31] C. Pirola, C.L. Bianchi, A. Di Michele, P. Diodati, S. Vitali, V. Ragaini, Catalysis Letters 131 (2009) 294–304.
[32] R.A. Friedel, R.B. Anderson, Journal of the American Chemical Society 72 (1950) 1212–1215.
[33] Y. Yin, W. Xu, R. DeGuzman, S.L. Suib, C.L. O'Young, Inorganic Chemistry 33 (1994) 4384–4389.
[34] M.J. Keyser, R.C. Everson, R.L. Espinoza, Applied Catalysis A 171 (1998) 99–107.
[35] J. Gaube, H.F. Klein, Applied Catalysis A 350 (2008) 126–132.
[36] F.M. Gottschalk, G.J. Hutchings, Applied Catalysis A 51 (1989) 127–139.
[37] T.Z. Li, Y. Yang, Z.C. Tao, H.J. Wan, X. An, C.H. Zhang, H.W. Xiang, Y.W. Li, Journal of Natural Gas Chemistry 16 (2007) 354–362.
[38] J.C. Zhang, X.H. Guo, W.L. Cao, Journal of Natural Gas Chemistry 16 (2007) 377–381.
[39] J.P. den Breejen, P.B. Radstake, G.L. Bezemer, J.H. Bitter, V. Froseth, A. Holmen, K.P. de Jong, Journal of the American Chemical Society 131 (2009) 7197–7203.
[40] B.C. Shi, R.J. O'Brien, S.Q. Bao, B.H. Davis, Journal of Catalysis 199 (2001) 202–208.
[41] H. Pechler, H. Schulz, M. Elstner, Brennstoff-Chemie 48 (1967) 78–87.
[42] W.K. Hall, R.J. Kokes, P.H. Emmett, Journal of the American Chemical Society 82 (1960) 1027–1037.
[43] R.J. Madon, E. Iglesia, Journal of Catalysis 139 (1993) 576–590.
[44] A.Y. Khodakov, A. Griboval-Constant, R. Bechara, V.L. Zholobenko, Journal of Catalysis 206 (2002) 230–241.
[45] R.L. Zhang, J. Chang, Y.Y. Xu, L.R. Cao, Y.W. Li, J.L. Zhou, Energy and Fuels 23 (2009) 4740–4747.
[46] W. Zimmerman, D. Bukur, S. Ledakowicz, Chemical Engineering Science 47 (1992) 2707–2712.
[47] E. de Smit, F. Cinquini, A.M. Beale, O.V. Safonova, W. van Beek, P. Sautet, B.M. Weckhuysen, Journal of the American Chemical Society 132 (2010) 14928–14941.
[48] H. Schulz, T. Riedel, G. Schaub, Topics in Catalysis 32 (2005) 117–124.
[49] C.G. Visconti, L. Lietti, E. Tronconi, P. Forzatti, R. Zennaro, E. Finocchio, Applied Catalysis A 355 (2009) 61–68.
[50] C.F. Huo, Y.W. Li, J.G. Wang, H.J. Jiao, Journal of the American Chemical Society 131 (2009) 14713–14721.
[51] J.T. Kummer, T.W.d. Witt, P.H. Emmett, Journal of the American Chemical Society 70 (1948) 3632–3643.
[52] B.H. Davis, Fuel Processing Technology 71 (2001) 157–166.
[53] H. Kolbel, K.D. Tillmetz, Journal of Catalysis 34 (1974) 307–316.
[54] S.D. Senanayake, D. Stacchiola, P. Liu, C.B. Mullins, J. Hrbek, J.A. Rodriguez, The Journal of Physical Chemistry C 113 (2009) 19536–19544.